Journal of
Materials Chemistry C

ROYAL SOCIETY
OF CHEMISTRY

REVIEW

View Article Online
View Journal | View Issue

Check for updates

Cite this: *J. Mater. Chem. C*, 2022, **10**, 2400

Emerging materials for circularly polarized light detection†

Xiaobo Shang,‡[a] Li Wan, ‡[b] Lin Wang,[a] Feng Gao [b] and Hanying Li *[a]

Received 2nd September 2021,
Accepted 26th October 2021

DOI: 10.1039/d1tc04163k

rsc.li/materials-c

Detecting circularly polarized light (CPL) signals is the key technique in many advanced sensing technologies. Over recent decades, many efforts have been devoted to both the material design and the device engineering of CPL photodetectors. CPL detectors with different sensing wavelengths have distinct applications in bio-imaging, drug discovery, and information encryption. In this review, we first introduce the working principle of state-of-the-art CPL photodetectors followed by a general material design strategy. We then systematically summarize the recent progress on the chiral materials developed for CPL detection, including inorganic metamaterials, organics, hybridized materials, *etc.* We compare and analyse the photocurrent dissymmetry factors of these systems and provide perspectives on strategies to improve the dissymmetry factors and extend the detection wavelength. We believe that the information we include in this review would attract broader interest from researchers working on different aspects of organic and hybridized semiconductor materials and devices.

Introduction

The circular polarization of light, in classic electrodynamics, defines a state where the electromagnetic field of the wave rotates in a plane perpendicular to its propagation direction. When a light beam is circularly polarized, in addition to the energy information (*i.e.*, wavelength), the photons would carry a spin angular momentum, which is directed along the beam axis. Therefore, circularly polarized light (CPL) is also called spin-polarized light when emphasizing such spin information. Circularly polarized electromagnetic wave or CPL has been widely used in a wide range of applications including satellite communication and 5G techonlogies,[1] quantum optics,[2] bio-imaging,[3] and many advanced sensing technologies.[4,5] To sense these external CPL signals, a matched CPL detector is required to convert them to electrical signals. A routinely used strategy is combining polarization-insensitive photodetector

---

[a] *MOE Key Laboratory of Macromolecule Synthesis and Functionalization, Department of Polymer Science and Engineering, Zhejiang University, Hangzhou, P. R. China. E-mail: hanying_li@zju.edu.cn*

[b] *Department of Physics, Chemistry and Biology (IFM), Linköping University, Linkoping, 58184, Sweden*

† Dedicated to Prof. Daoben Zhu on the occasion of his 80th birthday.

‡ Xiaobo Shang and Li Wan equally contributed to this work.

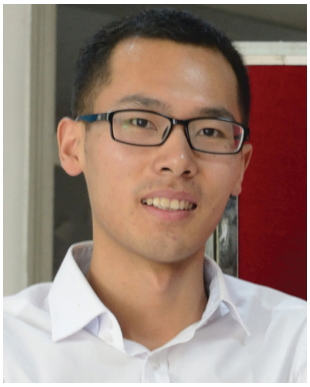

Xiaobo Shang

Xiaobo Shang received his PhD from Zhejiang University in 2014 and joined Prof. Joon Hak Oh's group as a postdoctoral researcher and then a research assistant professor at Pohang University of Science and Technology and Seoul National University, respectively, in 2014 and in 2018. He became a research associate at Oxford University from 2019 to 2020. He is currently a visiting scholar in Prof. Hanying Li's group. He mainly focuses on synthesis and self-assembly of chiral materials for chiral optoelectronics and various sensors.

Li Wan

Li Wan started working on chiral materials since 2017 when he joined the Campbell and Fuchter group at Imperial College London. He was focusing on circularly polarized light-emitting diodes and received his PhD in 2020. He is now a postdoctoral researcher in Linköping University working with Prof. Feng Gao. He is currently working on chiral materials including organics and perovskite materials and their applications in circularly polarized light photodetectors and emitting devices.

(*e.g.*, silicon photodetectors) and external optics consisting of a phase retarder (*e.g.*, quarter wave plates) and a linear polarizer or other polarization manipulation elements. The elliptically polarized light is first converted to linearly polarized light and then analyzed by the linear polarizer and the photodetector. Commercially available circularly polarized spectrofluorometers, as an example, utilize the photoelastic modulator as the phase retarder and birefringence modulator.[6] To miniaturize the devices, portable and low energy-consuming CPL detectors can be built based on materials that are directly sensitive to CPL.

Depending on how light interacts with the materials, a chiroptical response could result from the differential absorption, reflection, and scattering of left-handed (LH) and right-handed (RH) CPL. Since when the very first CPL detector directly using 1-aza-[6]helicene molecules as the active layer was reported in 2013, recent solution-processed CPL detectors are based on the differential absorption of LH and RH CPL [*i.e.*, circular dichroism (CD)] in the chiral active layers. To date, a wide range of chiral materials have been applied in the CPL photodetectors including inorganic metamaterials,[7] helicenes,[8] chiral polymeric materials,[9] and most recently chiral perovskites.[10]

Lin Wang

Lin Wang received her M.S. degree from Nankai University in 2020. She is currently a PhD candidate under the supervision of Prof. Hanying Li at the Department of Polymer Science and Engineering, Zhejiang University, China. Her research focuses on chiral organic–inorganic hybrid perovskite single crystals for circularly polarized light photodetectors.

With the rapid development of new structures of chiral molecules and crystals, studies on CPL detectors have attracted increasing interest in both scientific research and industry. In this review, we systematically summarize the recent progress of chiral materials, in particular, chiral organic and hybrid organic–inorganic materials, developed for CPL detection and presents our perspectives on open questions in this research area. We hope that the information included in this review not only covers the state-of-the-art CPL detection studies, but also could inspire other researchers to join this fast-growing research field.

Intrinsic chirality and CPL detection

Photodetectors including CPL photodetectors are devices with the ability to convert light signals to electrical signals. The added value of the embedded chiral materials is to enable the devices to sense and differentiate the circular polarization of the incident light. There are three commonly used device structures for the state-of-the-art organic and hybridized photodetectors – vertical two-terminal photodiodes, horizontal two-terminal photoconductors, and horizontal three-terminal phototransistors.[11,12] Since the detailed device operation and light detecting mechanisms for general photodetectors have been summarized and reviewed elsewhere,[11,12] we here focus on the working principle of the CPL detection in these devices.

The key figure of merit of the CPL photodetector is the photocurrent dissymmetry factor (g_{ph}) which is defined as:

$$g_{\mathrm{ph}} = \frac{I_{\mathrm{L}} - I_{\mathrm{R}}}{\frac{1}{2}(I_{\mathrm{L}} + I_{\mathrm{R}})} \tag{1}$$

where I_{L} and I_{R} are the photocurrent of the detectors under the illumination of LH and RH CPL, respectively. Similarly, replacing photocurrent with responsivity of the device, we could calculate the responsivity dissymmetry factor g_{R}.

In a photovoltaic device such as solar cells and photodiodes, the photocurrent is generated by the absorption of the active

Feng Gao

Feng Gao is a professor and Wallenberg Academy Fellow at Linköping University in Sweden. He received his PhD from the University of Cambridge (UK) in 2011, followed by a Marie Curie postdoc fellowship at Linköping University. His group currently focuses on research into solution-processed energy materials and devices, mainly based on organic semiconductors and metal halide perovskites.

Hanying Li

Hanying Li is a professor at the Department of Polymer Science and Engineering, Zhejiang University, China. In 2009, he completed his PhD degree at Cornell University in materials science and engineering (advisor: Prof. Lara A. Estroff). After postdoctoral work on organic electronics at Stanford University (Prof. Zhenan Bao's group), he moved to Zhejiang University in 2011. His current research mainly focuses on bio-inspired single-crystal/gel composites, polymer crystallization and organic-single-crystal-based electronic and optoelectronic devices.

layer materials. Therefore, in a CPL photodetector, g_{ph} is strongly dependent on the g_{abs}.

Experimentally, g_{abs} can be extracted from CD spectra using the following equation:[13]

$$g_{\text{abs}} = \frac{\Delta A}{A} \tag{2}$$

where ΔA and A are the differential and average absorbance of LH and RH CPL, respectively. g_{abs} has a range of $-2 \leq g_{\text{abs}} \leq 2$. $g_{\text{abs}} = 2$ or $g_{\text{abs}} = -2$ indicate the material is fully LH CPL absorbing or RH CPL absorbing. For a system in which $\Delta A \ll 1$, ellipticity (θ) can be empirically derived from a simplified equation as follows,[14]

$$\theta(\text{degree}) = \Delta A\left(\frac{\ln 10}{4}\right)\left(\frac{180}{\pi}\right) = 32.98\ \Delta A \tag{3}$$

where ΔA can be directly measured using a CD spectrometer.

For the quantitative analysis of solid-state samples, reflectance-corrected absorbance (A_{corr}) could be used to replace the measured A in eqn (2) and the true absorption dissymmetry factor (g_{true}) can be written as:[15]

$$g_{\text{true}} = \frac{\Delta A}{A_{\text{corr}}} \tag{4}$$

which is a thickness-independent value.

It is also worth emphasizing that the above-mentioned CD and chiroptical response should manifest in absorption only (*i.e.*, non-scattering and non-reflectance) and we should not confuse the aforementioned CD with the Bragg reflection of CPL in mesoscopic materials.[16] Although structurally chiral materials such as liquid crystal materials and metamaterials could demonstrate a chiroptical response, and the term 'CD' is frequently used in these areas, the chiroptical response of these materials stems from the selective reflection of CPL in the chiral media. The central wavelength (λ_{Bragg}) of the Bragg regime is given by:

$$\lambda_{\text{Bragg}} = \text{np} \tag{5}$$

where n is the refractive index of the material and p is the pitch of the helical nanostructures. To identify the spectroscopic difference between intrinsically chiral materials and structurally chiral materials, chiroptical response in both transmission and reflection mode should be measured.[16] Structurally chiral materials exhibit a chiroptical response (or CD) in both measurement geometries while intrinsically chiral materials exhibit CD in the transmission mode only.

Concerning the electronic transition associated with the absorption process of the intrinsically chiral material, the theoretical dissymmetry factor is described as below,[17]

$$g = \frac{4R}{D} = \frac{4\boldsymbol{\mu}\cdot\boldsymbol{m}}{|\boldsymbol{\mu}|^2+|\boldsymbol{m}|^2} = \frac{4|\boldsymbol{\mu}|\cdot|\boldsymbol{m}|\cos\theta}{|\boldsymbol{\mu}|^2+|\boldsymbol{m}|^2} \tag{6}$$

where R is the rotatory strength, D is the dipole strength, $\boldsymbol{\mu}$ and $\boldsymbol{m}$ are the electric and magnetic transition dipole moments, and θ is the relative angle between $\boldsymbol{\mu}$ and $\boldsymbol{m}$. In an isolated molecular system, the magnitude of the dissymmetry factor is limited by $|\boldsymbol{m}|$, since in semiconducting materials, $|\boldsymbol{m}|$ is usually 3 orders of magnitude smaller than $|\boldsymbol{\mu}|$.[17]

When it comes to the aggregated or solid-state systems, the coupled chromophores could exhibit a much larger chiroptical response due to exciton coupling.[18–20] As well-illustrated in several reviews by the Di Bari group,[18,21] the excited state of the chromophores exhibiting intense π–π* interaction is split into two energy levels, giving rise to LH and RH CPL absorption and emission.[22] Systems featuring this process (*i.e.*, Davydov splitting) show clear bisignate CD peaks and two opposite Cotton effects.[22] The rotatory strength of coupled chromophores (*e.g.*, chromophores 1 and 2) is therefore proportional to the electric transition dipole strength of the individual chromophore, which can be described as follows,

$$R_{1,2} \propto \pm\, \boldsymbol{r}_{1,2}\cdot\boldsymbol{\mu}_1 \times \boldsymbol{\mu}_2 \tag{7}$$

where $\boldsymbol{r}$ is the interchromophoric distance vector between 1 and 2. $\boldsymbol{\mu}_1$ and $\boldsymbol{\mu}_2$ are electric transition dipole moments of each individual chromophore.

Although directly enhancing magnetic transition dipole strength in chromophores could effectively improve dissymmetry factors, it also requires more twisted molecular structures in terms of molecular design, which could possibly decrease the mobility of the semiconducting materials. In this case, designing chiral systems exhibiting strong exciton coupling would be an alternative design approach to achieving a high dissymmetry factor without sacrificing semiconductor properties.

Inorganic materials

Telecommunication is one of the key applications of CPL, where the use of cross-polarized electromagnetic waves could double the efficiency of the information transmission, and the states of circular polarization are unchanged relative to the orientation of antenna in space.[1] Although a near infrared (NIR) source can be used in short-distance transmission, the fibre losses are relatively high in the NIR region.[23] Longer distance telecommunication technologies utilize wavelengths from 1260 nm to 1675 nm,[7] and unfortunately, the optical band gap of the organic and hybridized materials can hardly reach this wavelength range. For CPL detection over 1000 nm, structurally chiral inorganic materials are more commonly used.

The detection mechanisms of these materials are not associated with the electronic transition of the active layer and are beyond the scope of this review. Here, we only use a few examples to explain the working principles and highlight the CPL detection wavelength of these materials since they are good supplementary materials for organic and hybridized CPL detectors.

Metamaterials are a group of materials with artificially engineered structures and near-perfect absorption coefficients. When chiral nanostructures or structurally chiral media are embedded, the metamaterials could demonstrate chiroptical response. Li *et al.* fabricated a metamaterial comprising of a plasmonic array, a dielectric layer and a metal reflector (Fig. 1a).[7]

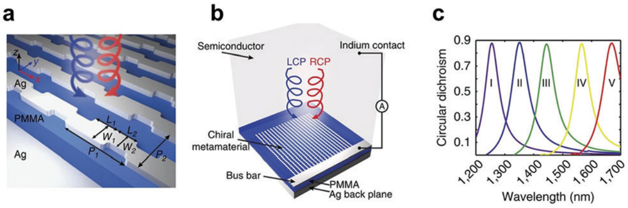

Fig. 1 (a) Schematic of the chiral metamaterial consisting of a chiral plasmonic meta-molecule array, dielectric spacer, and metal backplane. The thicknesses of the meta-molecules, dielectric spacer and the metal backplane are 40, 160 and 100 nm, respectively. (b) A schematic of the CPL detector consisting of a chiral metamaterial integrated with a semiconductor that serves as a hot electron acceptor. The Ohmic contact on Si is formed by soldering indium. The circuit is formed by wire bonding to the silver bus bar and indium. (c) CD as a function of resonator size. Dimensions of the structures (*I*–*V*) are as follows: L_1 = 115, 125, 130, 150 and 160 nm; L_2 = 95, 105, 120, 130 and 140 nm; W_1 = 110, 115, 120, 120 and 140 nm; W_2 = 85, 85, 90, 90 and 100 nm; P_1 = 305, 335, 370, 410 and 440 nm; P_2 = 230, 235, 240, 240 and 260 nm, respectively. The other dimensions are the same as in (a). Reproduced with permission from ref. 7. Copyright 2015, Nature Publishing Group.

Z-shaped silver nano-antennas were fabricated and defined on top of the PMMA resist spacer using electron beam lithography. Strong chiroptical effect stems from the destructive interference of one handedness CPL and constructive interference of the opposite handedness within reflective surfaces. They also combine enantiomeric Z-shape plasmonic materials with a hot electron photodetector (Fig. 1b). As a result, the device can effectively distinguish between LH and RH CPL with a polarization discrimination ratio of 3.4, which is equivalent to a g_{ph} of 1.09. The detection wavelength of metamaterials can be further extended by varying the dimension of the metamolecular arrays (Fig. 1c)[24,25] or changing the shape of the patterned plasmonic materials.[26]

Apart from metamaterials, other materials exhibiting strong Bragg reflection of CPL could also be applied in CPL detectors. By using a glancing angle deposition method, Lee *et al.* grew chiral oxide films on a tilt rotating silicon substrate.[27] With this chiral inorganic layer, the silicon detector could sense CPL with a g_{ph} of up to 0.30. By tuning the pitch length and/or refractive index of the materials, the chiral oxide layer can selectively reflect CPL with a specific handedness at a central wavelength of Bragg reflection. To achieve a chiroptical response in thin-films and devices, micrometre-thick films or complicated nanofabrication techniques are required for these intrinsically achiral materials. In the following sections, we will introduce organic and hybridized chiral materials which can be directly used as the active layer in a photodetector by a much simpler solution-process method.

Organic chiral semiconducting materials

Small molecules for CPL detection

In terms of processability, π-conjugated organic materials with intrinsic chirality are more suitable for applications in CPL detection due to their light weight, tunable chemical structures, and compatibility with flexible substrates. Owing to the coherently chiral molecular structures, helicenes have been considered as promising candidates for chiral optoelectronics.[8,28] The aromatic rings in helicenes are angularly annulated, giving rise to helical geometry.

In 2013, Yang *et al.* reported the first organic field-effect transistor (OFET) for CPL detection directly using enantiomerically pure 1-aza-[6]helicene (**1**, Fig. 2a).[8] For OFETs using enantiopure (*P*)-**1**, the off-current was increased by an order of magnitude from 10^{-10} A to 10^{-9} A by illuminating RH CPL (λ = 365 nm, 10 mW cm^{-2}) with an on/off ratio of 1×10^3 and a mobility of 1×10^{-4} cm^2 V^{-1} s^{-1}, but no obvious change in the off-current under the illumination of LH CPL (Fig. 2b). The selective increase of the off-current is related to excitons generation within (*P*)-**1** molecules close to the transistor channel. With RH CPL illumination, more excitons dissociated into holes and electrons to give rise to greater photogenerated leakage current. However, when increasing the drain voltage, this effect is less obvious, and for (*P*)-**1** transistors, the on-state photocurrent under LH and RH CPL is almost identical (Fig. 2b). This also indicates that the best working regime of CPL detection is the off-state of the phototransistor rather than the on-state. Although the batch-to-batch difference and the crystal morphology stability have to be improved for these materials,[29] this pioneering work opens up the door for CPL detection directly using chiral organic semiconducting materials.

Enhancing the chiroptical response of helicenes remains a significant challenge and low g_{abs} limits the practical applications of (*P*/*M*)-**1**. Therefore, we have to consider approaches to further increasing the g_{abs} of helicene mateirals.[30] One straightforward way is to extend the conjugation of the helicenes along its helix (*i.e.*, in the *ortho*-fused fashion) and theoretical studies have demonstrated that the g_{abs} of single-handed [*n*]carbohelicenes can be increased with the greater number of aromatic rings (*n*).[31] So far, the longest [*n*]carbohelicenes has been [16]helicene, which was synthesized by Fujita and co-workers in 2015 with an extremely low yield of 7% in the final photocyclization step.[32] Another effective method to increase g_{abs} in helicene chemistry is the lateral extension of π-conjugated

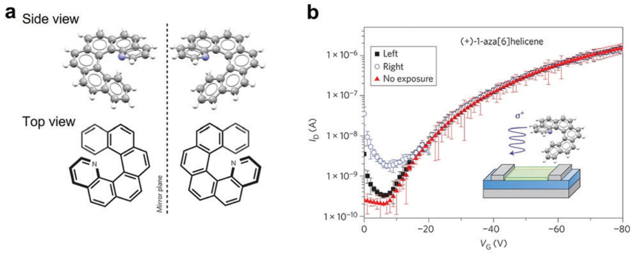

Fig. 2 (a) Molecular structures of (*M*)-**1** and (*P*)-**1**. (b) Transfer characteristics of (*P*)-**1** OFET upon exposure to LH (black squares) and RH (blue circles) CPL. The OFET transfer characteristics were recorded at V_D = −60 V. Insets: Molecular structure of (*P*)-**1** and the sign of the CPL (RH (σ^+) or LH (σ^-)) to which the OFETs respond. Reproduced with permission from ref. 8. Copyright 2013, Nature Publishing Group.

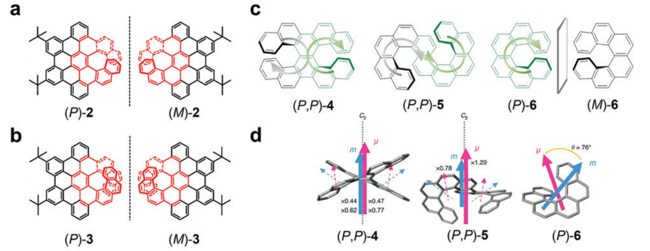

Fig. 3 (a) Molecular structures of (*P*/*M*)-**2**. (b) Molecular structures of (*P*/*M*)-**3**. Reproduced with permission from ref. 33. Copyright 2021, American Chemical Society. (c) Molecular structures of double helicene (*P*,*P*)-**4** and (*P*,*P*)-**5** originated from parent single helicene (*P*)-**6**. (d) Schematic representation of electric ($\boldsymbol{\mu}$) and magnetic ($\boldsymbol{m}$) transition dipole moments of the ^1B_b band for X-shaped and S-shaped double hexahelicenes (*P*,*P*)-**4** and (*P*,*P*)-**5**, with the magnitudes relative to parent (*P*)-**6**, calculated at the RI-CC2/def2-TZVPP level. Reproduced with permission from ref. 34. Copyright 2018, Nature Publishing Group.

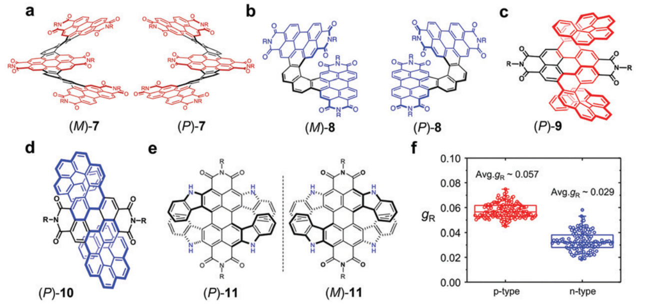

Fig. 4 (a)–(e) Molecular structure of PDI-helicenes (*M*/*P*)-**7**, (*M*/*P*)-**8**, Reproduced with permission from ref. 36. Copyright 2018, American Chemical Society. (*P*)-**9**, (*P*)-**10**, Reproduced with permission from ref. 40. Copyright 2020, American Chemical Society and (*P*/*M*)-**11**; (f) quantitative analysis results of g_{R} of four (*P*)-**11** OFET devices under CPL irradiations (λ = 635 nm). Reproduced with permission from ref. 41. Copyright 2021, Nature Publishing Group.

systems. π-extended [7]helicene (**2**, Fig. 3a) and [9]helicene (**3**, Fig. 3b) through regioselective cyclodehydrogenation in high yield was reported by Qiu *et al.* in 2021.[33] An increase in g_{abs} of **3** by a factor of 10 compared with that of **2** was due to its higher $|\boldsymbol{m}|$, lower $|\boldsymbol{\mu}|$, and smaller θ. Besides, extending the helical conjugation by forming a double helicene with X-shape (not yet developed, (*P*,*P*)-**4**) and S-shape ((*P*,*P*)-**5**) were estimated to double the CD compared to their parent single helicene (*P*)-**6**. The C_2-symmetry element along the helical axis of (*P*,*P*)-**4** and (*P*,*P*)-**5** (dashed line) parallel-aligns the $\boldsymbol{\mu}$ and $\boldsymbol{m}$ moments of the ^1B_b transition, giving rise to a maximized $\cos\theta$ value (eqn (6)) and extraordinary CD intensities.[34]

For spectroscopic applications of CPL detectors, a strong chiroptical response is only one of the prerequisites for active layer materials, they also have to cover a wide range of wavelengths. Due to the twisted structures of helicenes, their absorption band is largely restricted to the UV region. Perylene diimides (PDIs) and their derivatives have been extensively studied in organic optoelectronics due to their versatile structures and thermo- and opto-stability.[35] Therefore, PDI-based helicenes with impressive chiroptical properties have attracted great attention recently. PDI moieties could help helicene structures increase the g_{abs}, and most importantly, can extend the absorption band of helicenes from the UV to visible-NIR region. Schuster *et al.* synthesized the shape-persistent π-helix-of-helicenes **7** *via* iterative palladium-catalyzed cross-coupling and intramolecular oxidative photocyclizations.[36] The $|g_{\text{abs}}|$ of **7** was increased by 7.2-fold and 5.9-fold compared with that of **8** at 355 nm and 401 nm, respectively. With more units embedded in the helicene structures, large exciton-coupling CD signals could be observed.[37–39]

Wang's group recently reported a series of double [8]helicenes (**9** and **10**, Fig. 4c and d), which exhibit the highest g_{abs} and g_{lum} of double carbohelicenes so far. The superhelicene (*P*)-**9** exhibited a $|g_{\text{abs}}|$ of 0.012 at 411 nm, while (*P*)-**10** showed a maximum $|g_{\text{abs}}|$ of 7.6×10^{-3} at 403 nm.[40] A similar double helicene structure has been recently applied in solid-state CPL photodetectors. Zhang *et al.* fabricated a phototransistor using a PDI double-[7]heterohelicene ((*P*/*M*)-**11**) demonstrating a high photoresponsivity of 450 and 120 mA W^{-1} in both p- and n-type regimes under NIR light irradiation.[41] In the solution state CD spectra, g_{abs} = 0.014 was obtained at λ = 628 nm. More importantly, the CD spectra could reach a wavelength beyond 700 nm, which is a great extension of the CPL detection wavelength range for helicene-based materials. When illuminating the device with LH CPL (λ = 635 nm), (*P*)-**11**-based OFETs exhibited a higher photocurrent, while (*M*)-**11** OFETs showed a mirror response. g_{R} values of (*P*)-**11** OFETs were estimated to be +0.057 and +0.029 in p-type and n-type real-time CPL detection, respectively (Fig. 4f). The relatively larger g_{R} compared to g_{abs} may originate from the synergistic effect of the enhanced photocurrent difference from photomultiplication phenomena by the applied gate bias and the spin-dependent carrier transport/collection effect due to the optical selection rules. Although it was a great improvement that the absorption band of a PDI double helicene could reach the NIR region (λ = 730 nm), the absorption coefficient at the NIR region is much lower than that at the UV region, limiting the photocurrent generation in OFETs. Developing chiral materials with strong NIR absorption remains a significant challenge in the area of CPL detection.

In terms of the development of photovoltaic materials, fullerenes were used as electron acceptors prior to non-fullerene materials including PDIs.[43] Recently, desymmetrized fullerenes were separated using chiral high-performance liquid chromatography. Shi *et al.* separated ten pairs of enantiomers from the 19 structural isomers of bis-PC$_{61}$BM.[42] Enantiomers of **12** and **13** were selectively used for CPL detection on bottom-gate bottom-contact phototransistors (Fig. 5a and b). Under illumination of CPL at 405 nm, g_{ph} of (*anti*,*R*)-**12** and (*R*,*R*,^{f,s}*A*)-**13** were obtained as 1.27 ± 0.06 and −0.26 ± 0.18, respectively, which are significantly larger than their g_{abs} ($<$0.005). The author proposed two cooperative mechanisms: CP selective photogeneration of holes accumulated at the source electrode to reduce the barrier to electron injection and the CP selective photogeneration of electrons in the channel to increase the

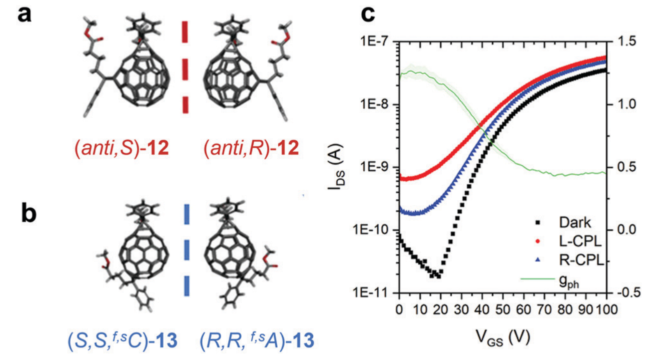

Fig. 5 (a) and (b) Molecular structures of enantiopure bis-$PC_{61}BM$ (*anti,S*/*R*)-**12** and (*S,S*/*R,R*,^{f,s}*C*/*A*)-**13**. (c) Variation of transfer curves of (*anti,R*)-**12** upon exposure to LH and RH CPL (95 mW cm^{-2}), compared to curves in the dark. V_D = 20 V. Dissymmetry factors for the photocurrent generation (g_{ph}) and its associated error are given by the green curve and shaded area, respectively. Reproduced with permission from ref. 42. Copyright 2021, Wiley-VCH.

majority of carrier density. Similar to the phototransistor reported using (*P*/*M*)-**1**,[8] the maximum g_{ph} of these fullerene based phototransistors appears at the off-state of the transistor (Fig. 5c) and the photocurrent is limited by the low absorption coefficient of fullerenes as well as the insufficient charge separation in the absence of electron donating materials.

Chiral polymeric systems for CPL detection

Instead of using neat helicene directly as the active materials, recent studies show that it can also be used to induce chirality in polymeric systems.[13,19,44,45] Such systems were pioneeringly studied in the Campbell and Fuchter group, although they were originally studied in CP light emitting diodes.[44] Yang *et al.* firstly reported a blend system comprising of 1-aza-[6]helicene (**1**, Fig. 2a) and an achiral polymer poly[(9,9-di-*n*-octylfluorenyl-2,7-diyl)-*alt*-(benzo[2,1,3]thiadiazol-4,8-diyl)] (F8BT, **14**) in 2013.[44] With 7% of (*P*/*M*)-**1** additive, a strong CD signal (∼300 millidegree) was obtained at the polymer absorption band around 450 nm. The chiroptical response could be further enhanced by increasing the loading ratio of the (*P*/*M*)-**1** additive. It has also been proved by the following studies that this strategy can be widely applied in other polyfluorene systems, such as poly(9,9-di-*n*-octylfluorenyl-2,7-diyl) (PFO, **15**) and poly(9,9-dioctylfluorene-*alt*-bithiophene) (F8T2, **16**).[19,45,46]

The annealed **16**:(*P*)-**1** films exhibit strong CD signals >20 000 mdeg at λ = 498 nm,[46] which would be suitable for CPL detection at this wavelength. Based on previous studies of chiral polymer blends, Ward *et al.* reported a bilayer chiral organic photodiode (ITO/PEDOT/**16**:(*P*)-**1**/C_{60}/Al), which was constructed for CPL detection with g_{ph} of up to 0.12 at λ = 455 nm.[47] Owing to the bilayer device structure, the polymer donor mainly acts as a CPL 'filter' for thicker polymer films and the charge separation occurs within the donor acceptor (C_{60}) interface. The resulted g_{ph} has an opposite sign to the g_{abs} of the polymer blends. Similar results and device optics modelling have been reported by the Meskers Group where a chiral side chain polyfluorene ((*S*)-**17**) was used as the chiral polymer donor.[9] It was also the very first reported CPL photodiode. The authors observed a polymer layer thickness dependent g_{ph}. In the devices with a thinner polymer donor layer (∼80 nm), the g_{ph} of short-circuit current was a positive value of $+0.7 \times 10^{-2}$. However, for thicker film (136 nm), the photodiode exhibits a negative g_{ph} of -1.7×10^{-2} (λ = 543 nm). The author proposed the distinct mechanisms for the polymer-thickness dependent g_{ph}: (i) for thinner polymer layer (∼80 nm), LH CPL could selectively reach the most active donor–acceptor interface in the device which produces the most photocurrent. (ii) For thicker polymer layers (>100 nm), the contribution of g_{ph} is determined mainly by the selectivity of the PEDOT:PSS/polymer interface. The majority of LH CPL is absorbed by the thick layer of polymer without generating effective photocurrent. In this case RH CPL is preferentially absorbed by the donor–acceptor interface and results in the larger photocurrent. Although these devices both demonstrate high CPL sensitivity, the photocurrent of these photodiodes is relatively low due to the less ideal donor–acceptor interface for fullerene blends.

Most recently, Liu *et al.* demonstrated a bulk heterojunction blend using a chiral analogue of diketopyrrolopyrrole (DPP)-based electron donor material ((*S,S,S,S*)-**18**) and $PC_{61}BM$.[48] DPP polymers are well-studied low band gap electron donor materials for fullerene-based photovoltaics. Although the neat donor thin films exhibit a large CD signal ∼250 mdeg, when adding $PC_{61}BM$, CD to ∼150 mdeg, with a g_{abs} of ∼0.012 at λ = 606 nm. This indicates that phase separation happening in fullerene-based photovoltaic bulk heterojunction has an impact on the helical molecular packing structure of chiral polymers. One alternative approach has been proposed by Schulz *et al.* where enantiomerically pure prolinol-derived squaraines (*R,R*)-**19** were used with $PC_{61}BM$ to form bulk heterojunction blends.[49] Owing to strong aggregations of squaraine molecules, the blends exhibit a g_{abs} of 0.08 in the presence of 60 wt% $PC_{61}BM$. With a bulk heterojunction device structure (ITO/MoOx/chiral blends/Al), the g_{ph} (∼0.1) has an identical sign to the g_{abs} of the chiral blends.

Apart from the bulk polymer thin film, chiral helical polythiopene (**20**, Fig. 6) nanowires could also be applied in CPL detecting devices.[50] The chiral nanowires were synthesized in the presence of a chiral solvent (*R*)-(+)-limonene and then blended with $PC_{61}BM$. The bulk heterojunction blends exhibit a $|g_{abs}|$ of 1.6×10^{-3} while the photodiode (ITO/ZnO/**20**:PCBM/MoO_3/Ag) fabricated demonstrates a $|g_{ph}|$ of 4.7×10^{-2} (λ = 532 nm) which is an order of magnitude higher than g_{abs}.

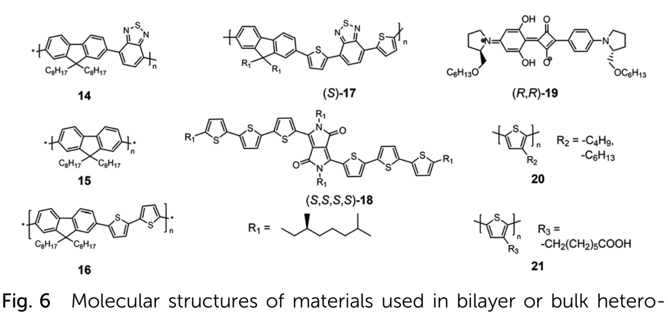

Fig. 6 Molecular structures of materials used in bilayer or bulk heterojunction photodiode cells.

The author suggested the amplified g_{ph} originates from chirality induced orbital angular momentum. RH CPL, in their claims, generates electron–hole pairs with weaker binding energy, giving rise to enhanced dissociation for a larger density of carrier, therefore, larger photodetectivity and photocurrent can be observed.

Another example of chiral polymer blends but using non-polyfluorene materials was reported by Kim *et al.* Polythiophene analogue poly[3-(6-carboxyhexyl)thiophene-2,5-diyl] (P3CT, **21**) was blended with (*R*/*S*)-1,1′-binaphthyl–2,2′-diamine (BN).[51] Phase separated bulk heterojunction blends of **21** and BN exhibit a significantly amplified chiroptical response due to the J-aggregation of BN with an ordered molecular structure, enhancing the exciton coupling by intra-and intermolecular dipole interactions. The photodiode using annealed blend films achieved a $|g_{ph}|$ ∼0.1 under the illumination at λ = 375 nm.

Other self-assembled systems

Chromophores with chiral pendant groups normally exhibit weak CD signals in the isolated state. After self-assembling into micro/nano-sized supramolecules, the chirality can be transferred from the chiral pendants to the whole system through both intra- and intermolecular interactions. Following this strategy, Shang *et al.* synthesized chiral perylene diimide (**22**) molecules, which could be self-assembled into nanostructures (Fig. 7).[52] For (*S*)-**22** nanowires, higher photocurrent was achieved upon exposure to LH CPL than RH CPL (λ = 460 nm, power = 50 μW cm^{-2}). Subsequently, they constructed quasi-2D chiral organic single crystals (ClCPDI-Ph) with parallelogram shape.[53] Through molecular surface n-doping using hydrazine, the electron mobility of the chiral crystals can surpass 1.0 cm^2 V^{-1} s^{-1}. Due to the formation of radical anions through n-doping, electron affinity was increased, resulting in a reduced band gap. Under irradiation of LH CPL or RH CPL (λ = 495 nm), the average responsivity dissymmetry factor g_R values were calculated as +0.129 and −0.120 for *S*- and *R*-enantiomerically pure doped single crystals, respectively.

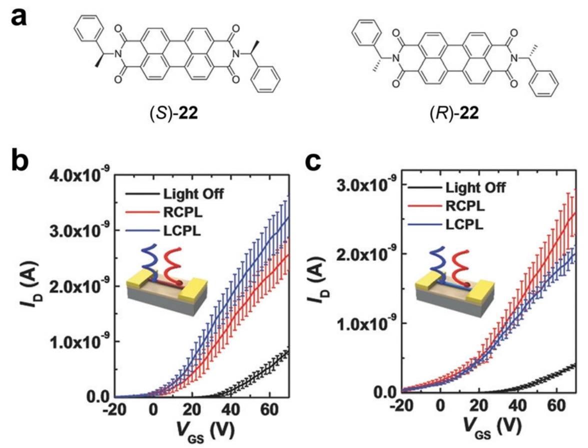

Fig. 7 (a) Molecule structures of chiral PDIs (*S*/*R*)-**22**. Transfer characteristics in the dark or under CPL illumination (λ = 460 nm, power = 50 μW cm^{-2}) for OFETs based on (b) (*S*)-**22** nanowires and (c) (*R*)-**22** nanowires. Reproduced with permission from ref. 52. Copyright 2017, Wiley-VCH.

Chiral perovskite materials

Owing to outstanding optoelectronic properties including high absorption coefficient, high defect tolerance, and excellent charge-carrier mobility, hybridized materials such as hybrid organic–inorganic perovskites (HOIPs) have been considered as promising candidates for a wide range of semiconductor applications.[54,55] Unlike organic systems, very limited stereogenic units could be embedded in perovskite structures. One of the straightforward methods is to incorporate stereogenic structures in organic cations to endow HOIPs with intrinsic chirality. The history, and other aspects of the chiral perovskite such as light-emitting properties, spintronics, and ferroelectrics have been reviewed elsewhere.[56] Here, we focus on the CPL detection using chiral perovskite materials.

0D chiral hybrids

To the best of our knowledge, zero-dimensional (0D) hybridized materials are rarely directly used as an active layer to perform CPL detection. Here we alternatively show an example where a heterojunction of 0D copper hybrids and single-walled carbon nanotube was use for CPL sensing (Fig. 8).[57] The 0D chiral copper chloride hybrids were synthesized using chiral ammonium (*R*/*S*)-methylbenzylammonium [(*R*/*S*)-MBA]. The hybrids [(*R*/*S*)-MBA]$_2$CuCl$_4$ exhibit CD signals for the ligand-to-metal charge transfer transition with a g_{abs} of ∼0.1. A high g_R of 0.21 was obtained in the chiral heterostructure-based CPL phototransistors, which is 4–5 times higher than g_{abs} at λ = 405 nm. In addition, an extremely high photoresponsivity of 452 A W^{-1} was achieved in the transistor due to the ultrafast electron transfer from hybrids absorber to the carbon nanotubes.

1D chiral OIHPs

The first report of one-dimensional (1D) chiral perovskite single crystals can be tracked back to 2003 when Billing *et al.* solved the single crystal structure of bis[(*S*)-β-phenethylammonium] tribromoplumbate.[58] Using similar cations, Tang *et al.* reported solution-processed CPL photoconductors based on highly oriented 1D [((*R*/*S*)-α-phenylethylamine)]PbI$_3$ [((*R*/*S*)-α-PEA)]PbI$_3$

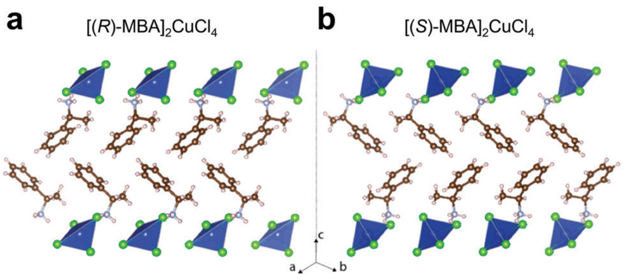

Fig. 8 Crystal structures of (a) [(*R*)-MBA]$_2$CuCl$_4$ and (b) [(*S*)-MBA]$_2$CuCl$_4$. Reproduced with permission from ref. 57. Copyright 2021, American Chemical Society.

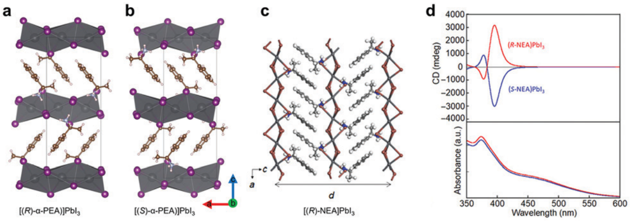

Fig. 9 Crystal structures of (a) $[((R)\text{-}\alpha\text{-PEA})]PbI_3$ and (b) $[((S)\text{-}\alpha\text{-PEA})]PbI_3$. Reproduced with permission from ref. 10. Copyright 2019, Nature Publishing Group. (c) $[(R)\text{-NEA}]PbI_3$. (d) CD and absorption spectra of $[(R)\text{-NEA}]PbI_3$ thin films. Reproduced with permission from ref. 59. Copyright 2020, Science AAAS.

films (Fig. 9a and b).[10] An impressive responsivity of 795 mA W^{-1} and detectivity of 7.1×10^{11} Jones under λ = 395 nm irradiance were reported. Both enantiomerically pure perovskite photodetectors exhibit a wavelength-dependent CPL response and a maximum g_R of ∼0.1 was achieved, which is much higher than the maximum g_{abs} (0.02). The authors proposed that this could originate from spin-dependent carrier transport and collection and large Rashba splitting in perovskites.

Concerning the polarization discrimination ratio between LH and RH CPL, the circular dichroism of the chiral perovskites still needs to be improved. Ishii *et al.* demonstrated CPL photodiodes based on helical 1D perovskite films.[59] By using chiral organic cations (*R*/*S*)-(1-(1-naphthyl)ethylammonium) [(*R*/*S*)-1-NEA] (Fig. 9c), the enantiopure perovskite thin films exhibit an exceptionally high CD of 3000 mdeg, which is higher than the CD values reported in any other perovskite system. Interestingly, the CD bands of the 1D structure show a clear bisignate feature which is similar to the coupled organic chromophores (Fig. 9d). The photodiode using $[(R)\text{-NEA}]PbI_3$ as an active layer exhibited the highest g_{ph} value (∼25.4) so far.

2D chiral OIHPs

Lead-halide perovskites. In 2006, Billing *et al.* reported a series of two-dimensional (2D) chiral perovskite structures.[60] However, no spectroscopic data was reported. Chiral perovskites have attracted great research interest since Moon and co-workers first explored the chiroptical properties of 2D chiral-perovskite films in 2017.[61] The first use of 2D chiral perovskite for sensitive CPL detection was reported by Li *et al.* in 2019.[62] In order to efficiently separate photogenerated carries, CPL detectors were constructed with *h*BN/chiral 2D perovskite $[((S)\text{- and }(R)\text{-}\alpha\text{-methylbenzylammoinium})]_2PbI_4$ crystals/MoS_2 heterostructures. (*R*/*S*)-α-Methylbenzylamine [(*R*/*S*)-MBA] is identical to (*R*/*S*)-α-PEA, but both are used in different literature reports.[10,62] Hereafter, we use MBA only in discussions for clarity. The photodetector could discriminate the polarization of CPL at λ = 518 nm. The calculated g_R was 0.09 at room temperature,[56] which is on a par with that of CPL detectors using 1D chiral perovskites. A peak responsivity of 0.45 A W^{-1} along with a detectivity of 2.2×10^{11} Jones was also achieved in a $[((R)\text{-MBA})]_2PbI_4$ microplate photodetector. Afterwards, Li's group developed an aqueous synthesis method for the same chiral 2D perovskite $[(R/S)\text{-MBA}]_2PbI_4$ single crystals.[63] Similarly, a CPL detector based on an exfoliated $[(R)\text{-(MBA)}]_2PbI_4$ microplate exhibited selectivity for CPL with an estimated g_R of 0.23.

In another study, Vardeny and co-workers reported in-plane and out-of-plane spin-related properties in 2D chiral $[(R/S)\text{-MBA}]_2PbI_4$ perovskite films.[64] A g_{ph} of 10% was obtained in the vertical diodes under the RH and LH CPL illumination at 7 K, which could originate from selective spin-transport induced by chirality-induced spin selectivity. A different mechanism is proposed for the in-plane photocurrent of planar photoconductors responding to CPL. In lateral devices, the authors proposed that the photocurrent difference was the result of a circular photogalvanic effect, which could be explained by Rashba splitting in the electronic bands.

Full-Stokes photodetectors are another promising optoelectronic device for full polarization detection, which is challenging as they require integrating multiple detectors with complicated photonic structures. In a recent work a Stokes-parameter photodetector was developed utilizing chiral 2D-perovskite $[(R/S)\text{-MBA}]_2PbI_4$ nanowires by a structural-engineering strategy.[65] High photocurrent anisotropy factors of 0.15 and 1.6 were obtained when under the excitation of 505 nm LH and RH CPL, and perpendicular linearly polarized light, respectively. Moreover, it is proved that Stokes-parameter photodetection can be realized with those chiral perovskite nanowires due to the matching trend of the measured photocurrent and theoretical absorption coefficients.

Lead-free perovskites. An everlasting challenge for lead-based perovskites is the toxic lead content, which has attracted a lot of novel designs of lead-free perovskite structures. Recently, the Luo group reported the first CPL photodetector using lead-free halide double perovskites, $[(R/S)\text{-}\beta\text{-methylphenethylammonium}]_4AgBiI_8\{[(R/S)\text{-}\beta\text{-MPA}]_4AgBiI_8\}$.[66] Specifically, the photodetector exhibits a unique bulk photovoltaic effect and a maximum g_{ph} of 0.3 for the self-power CPL detection at 520 nm, which might be ascribed to the polarized electronic spin activities induced by orbital angular momentum.

Quasi-2D chiral perovskites

In comparison to low-dimensional perovskites, the in-plane carrier transport mobility of quasi-2D perovskites could be enhanced due to the increased ratios of conductive inorganic slabs and less insulative organic spacers. Thus, the Yuan group reported a chiral quasi-2D perovskite thin-film CPL photodetector with enhanced detection performance using same chiral ligands as previously discussed for a lead-free perovskite.[67] The crystallization dynamics of the quasi-2D perovskite $[(R/S)\text{-}\beta\text{-MPA}]_2MAPb_2I_7$ film (MA = methylammonium) was modulated by solvent engineering and additional antisolvent. A parallel-oriented chiral quasi-2D perovskite film with homogenous energy landscape was acquired, which is of great importance in facilitating the in-plane carrier transport of the perovskite thin-film. The resultant responsivity for these photodetectors was as high as 1.1 A W^{-1}, the detectivity approached 2.3×10^{11} Jones, the g_{ph} reached 0.2 under the CPL illumination at λ = 532 nm.

The dimension of the perovskite could be further manipulated *via* a two-step solution-processed heteroepitaxy method.[68] Zhang *et al.* reported 2D/3D heterostructures based on $[(R/S)\text{-MPA}]_2\text{MAPb}_2\text{I}_7/\text{MAPbI}_3$ perovskites. The built-in electrical field was formed in the interface of the as-grown heterostructure crystal, enabling the reduced recombination probability for photogenerated carriers. The corresponding CPL photodetector exhibit amplified polarization discrimination ration between LH CPL and RH CPL with a g_R of 0.67 at zero bias, which is 6-fold larger than that of single-phased chiral quasi-2D perovskites [(*R*)-MPA] (g_R = 0.1).

Conclusions and perspectives

In this review, we provide a summary of the recent progress on CPL photodetectors based on intrinsically chiral semiconducting materials, including chiral small molecules, polymeric systems, and perovskites (Table 1). In organic systems, chiral polymer blends[47] exhibit the strongest chiroptical response in absorption, while some other small molecular systems give better g_{ph} in photodetector devices. For perovskite materials, a trade-off between charge transport properties and chirality is clear. 1D perovskites, so far, demonstrated the highest g_R of 1.84,[59] almost reaching the maximum value of g_R ($|g_R| = 2$), while higher dimensional perovskites usually demonstrate better optoelectronic properties.

In terms of the detecting wavelength, helicene derivatives mainly absorb at the UV region. With fused PDI structures, the absorption band could be extended to 730 nm,[41] however, the absorption coefficient is not sufficient to generate a high photocurrent. Nonetheless, this is the longest wavelength reported for photodetectors based on intrinsically chiral materials, while all other systems detect CPL below 650 nm. Although metamaterials featuring structurally chirality could be used to form nanostructures sensitive to CPL beyond 1000 nm, there is still a detection wavelength gap.

By analysing all reported CPL photodetectors, an interesting phenomenon can be found that the g_{ph} (or g_R) in most cases is larger than g_{abs}. In extreme cases, g_R is up to 3 orders of magnitude higher than g_{abs}. A few explanations were provided by different studies, including (1) difference in photocurrent generation caused by the differential absorption,[8,42,47] (2) difference in spin charge transport of the photo-induced charge carriers,[9,10,42,57,59] and (3) chirality induced orbital angular momentum.[50] However, so far, we have not yet had a consensus on which has the dominate contribution on the enhanced g_{ph}. In future studies, quantitative analysis on these aspects would certainly help us mechanistically understand the full working principle of CPL photodetectors.

In summary, although great efforts have been devoted to the material design and dissymetry factor improvement on the CPL photodetectors since the first CPL photodetector cell was reported in 2010,[9] we are still at the very early stages of this research area. New materials with extended detection wavelengths and large dissymetry factors are still needed. Developing the amplication mechanisms of g_{ph} will be very important for both theoretical and experimental studies of CPL photodetectors. We strongly believe that this fast developing area will attract more interest and could also inspire the development of

Table 1 Summary of chiral materials used for CPL photodetectors

Materials	Category	λ (nm)[a]	$\lvert g_{abs}\rvert$[b]	$\lvert g_{ph}\rvert$[c] (or $\lvert g_R\rvert$)	$\lvert g_{ph}\rvert/\lvert g_{abs}\rvert$
(*P*)-**1**[8]	Organic thin film	365	~10^{-3}	1.8	~1800
(*P*)-**11**[41]	Organic thin film	635	0.008	0.057	7.125
		730	0.002	0.010	5
(*anti*,*R*)-**12**[42]	Organic thin film	405	0.00027	1.27	~4700
(*R*,*R*,^{f,s}*A*)-**13**[42]	Organic thin film	405	0.002	0.26	130
16:(*P*)-**1**[47]	Organic thin film	455	0.2	0.12	0.6
(*S*)-**17**[9]	Organic thin film	543	0.056	0.017	0.3
(*S*,*S*,*S*,*S*)-**18**):$PC_{61}BM$[48]	Organic thin film	606	0.012	0.12	10
(*R*,*R*)-**19**:$PC_{61}BM$[49]	Organic thin film	543	0.08	0.1	1.25
20[50]	Organic nanowire	560	0.0016	0.047	29.375
21:BN[51]	Organic thin film	375	N/A	0.1	N/A
22[52]	Organic nanowire	460	~0.001	N/A	N/A
ClCPDI-Ph[53]	Organic crystal	495	N/A	0.129	N/A
$[(S)\text{-MBA}]_2\text{CuCl}_4$[57]	0D hybrid	405	~0.1	0.21	~2.1
$[(S)\text{-}\alpha\text{-PEA})]\text{PbI}_3$[10]	1D perovskite	395	0.02	0.1	5
$[(R)\text{-NEA}]\text{PbI}_3$[59]	1D perovskite	395	0.04	1.84	46.25
$[((R)\text{-MBA})]_2\text{PbI}_4$[62]	2D perovskite	518	N/A	0.09	N/A
$[((R)\text{-MBA})]_2\text{PbI}_4$[63]	2D perovskite	520	N/A	0.23	N/A
$[((R)\text{-MBA}]_2\text{PbI}_4$[64]	2D perovskite	486	N/A	0.1	N/A
$[(R)\text{-MBA}]_2\text{PbI}_4$[65]	2D perovskite	505	N/A	0.15	N/A
$[(R)\text{-}\beta\text{-MPA}]_4\text{AgBiI}_8$[66]	2D perovskite	520	~0.001	0.3	~300
$[(R)\text{-}\beta\text{-MPA}]_2\text{MAPb}_2\text{I}_7$[67]	Quasi-2D perovskite	532	N/A	0.2	N/A
$[(R)\text{-MPA}]_2\text{MAPb}_2\text{I}_7/\text{MAPbI}_3$[68]	Quasi-2D perovskite	520	N/A	0.67	N/A

[a] λ is the detection wavelength of the CPL photodetector, which in some references, are different from the peak absorption wavelength or peak g_{abs} wavelength. [b] Some g_{abs} values at a detection wavelength are re-calculated based on the absorption and CD spectra and eqn (3). The values might be different from the maximum g_{abs} reported or g_{abs} at absorption peak wavelengths. [c] Some g_{ph} values were calculated based on the *J*–*V* curves in the references.

other applications using chiral materials, such as circularly polarized emitting diodes,[69] encryption technologies,[70] spintronics,[71] and magneto-optoelectronics.[72,73]

Conflicts of interest

There are no conflicts to declare.

Acknowledgements

This work was supported by the National Key Research and Development Program of China (No. 2019YFE0116700 and 2019YFA0705900) funded by MOST, the National Natural Science Foundation of China (No. 51625304 and 51873182), and the Zhejiang Province Science and Technology Plan (No. 2021C04012) funded by the Zhejiang Provincial Department of Science and Technology. L. W. and F. G. acknowledge the financial support from the Knut and Alice Wallenberg Foundation (Dnr. KAW 2019.0082).

References

1 K. M. Mak, H. W. Lai, K. M. Luk and C. H. Chan, *IEEE Access*, 2014, **2**, 1521–1529.

2 J. F. Sherson, H. Krauter, R. K. Olsson, B. Julsgaard, K. Hammerer, I. Cirac and E. S. Polzik, *Nature*, 2006, **443**, 557–560.

3 V. V. Dremin, D. Anin, O. Sieryi, M. A. Borovkova, J. Näpänkangas, I. V. Meglinski and A. V. Bykov, in *Tissue Optics and Photonics*, ed. Z. Zalevsky, V. V. Tuchin and W. C. Blondel, SPIE, 2020, vol. 11363, p. 3.

4 S.-S. Lin, K. M. Yemelyanov, E. N. Pugh and N. Engheta, in *IEEE International Conference on Networking, Sensing and Control*, 2004, IEEE, 2004, vol. 1, pp. 216–221.

5 J. S. Tyo, M. P. Rowe, E. N. Pugh and N. Engheta, *Appl. Opt.*, 1996, **35**, 1855.

6 T. Harada, H. Hayakawa, M. Watanabe and M. Takamoto, *Rev. Sci. Instrum.*, 2016, **87**, 075102.

7 W. Li, Z. J. Coppens, L. V. Besteiro, W. Wang, A. O. Govorov and J. Valentine, *Nat. Commun.*, 2015, **6**, 8379.

8 Y. Yang, R. C. Da Costa, M. J. Fuchter and A. J. Campbell, *Nat. Photonics*, 2013, **7**, 634–638.

9 J. Gilot, R. Abbel, G. Lakhwani, E. W. Meijer, A. P. H. J. Schenning and S. C. J. Meskers, *Adv. Mater.*, 2010, **22**, E131–E134.

10 C. Chen, L. Gao, W. Gao, C. Ge, X. Du, Z. Li, Y. Yang, G. Niu and J. Tang, *Nat. Commun.*, 2019, **10**, 1927.

11 H. Ren, J.-D. Chen, Y.-Q. Li and J.-X. Tang, *Adv. Sci.*, 2021, **8**, 2002418.

12 K. J. Baeg, M. Binda, D. Natali, M. Caironi and Y. Y. Noh, *Adv. Mater.*, 2013, **25**, 4267–4295.

13 L. Wan, J. Wade, F. Salerno, O. Arteaga, B. Laidlaw, X. Wang, T. Penfold, M. J. Fuchter and A. J. Campbell, *ACS Nano*, 2019, **13**, 8099–8105.

14 H.-G. Kuball, T. Höfer and S. Kiesewalter, *Encyclopedia of Spectroscopy and Spectrometry*, Elsevier, 2017, pp. 217–231.

15 M. Schulz, J. Zablocki, O. S. Abdullaeva, S. Brück, F. Balzer, A. Lützen, O. Arteaga and M. Schiek, *Nat. Commun.*, 2018, **9**, 2413.

16 O. Arteaga, *Thin Solid Films*, 2016, **617**, 14–19.

17 P. M. L. Blok and H. P. J. M. Dekkers, *Chem. Phys. Lett.*, 1989, **161**, 188–194.

18 N. Berova, L. Di Bari and G. Pescitelli, *Chem. Soc. Rev.*, 2007, **36**, 914–931.

19 L. Wan, X. Shi, J. Wade, A. J. Campbell and M. J. Fuchter, *Adv. Opt. Mater.*, 2021, **9**, 2100066.

20 K. Swathi, C. Sissa, A. Painelli and K. G. Thomas, *Chem. Commun.*, 2020, **56**, 8281–8284.

21 G. Albano, G. Pescitelli and L. Di Bari, *Chem. Rev.*, 2020, **120**, 10145–10243.

22 N. Berova, N. Harada and K. Nakanishi, *Encyclopedia of Spectroscopy and Spectrometry*, Elsevier, 2017, pp. 539–557.

23 R. J. Essiambre, R. W. Tkach and R. Ryf, *Optical Fiber Telecommunications VIB: Systems and Networks*, Academic Press, 6th edn, 2013, pp. 1–43.

24 J. Peng, B. P. Cumming and M. Gu, *Opt. Lett.*, 2019, **44**, 2998.

25 Z. Chu, J. Zhou, X. Dai, F. Li, M. Lan, Z. Ji, W. Lu and X. Chen, *Adv. Opt. Mater.*, 2020, **8**, 1901800.

26 X. Shi, W. Xiao, Q. Fan, T. Zhou, W. Song, C. Zhang, Y. Zeng and W. Peng, *IEEE Sens. J.*, 2018, **18**, 9203–9206.

27 S. H. Lee, D. P. Singh, J. H. Sung, M. H. Jo, K. C. Kwon, S. Y. Kim, H. W. Jang and J. K. Kim, *Sci. Rep.*, 2016, **6**, 1–8.

28 H. Kubo, T. Hirose, T. Nakashima, T. Kawai, J. Hasegawa and K. Matsuda, *J. Phys. Chem. Lett.*, 2021, **12**, 686–695.

29 Y. Yang, B. Rice, X. Shi, J. R. Brandt, R. Correa da Costa, G. J. Hedley, D.-M. Smilgies, J. M. Frost, I. D. W. Samuel, A. Otero-de-la-Roza, E. R. Johnson, K. E. Jelfs, J. Nelson, A. J. Campbell and M. J. Fuchter, *ACS Nano*, 2017, **11**, 8329–8338.

30 J. L. Greenfield, J. Wade, J. R. Brandt, X. Shi, T. J. Penfold and M. J. Fuchter, *Chem. Sci.*, 2021, **12**, 8589–8602.

31 Y. Nakai, T. Mori and Y. Inoue, *J. Phys. Chem. A*, 2012, **116**, 7372–7385.

32 K. Mori, T. Murase and M. Fujita, *Angew. Chem., Int. Ed.*, 2015, **54**, 6847–6851.

33 Z. Qiu, C.-W. Ju, L. Frédéric, Y. Hu, D. Schollmeyer, G. Pieters, K. Müllen and A. Narita, *J. Am. Chem. Soc.*, 2021, **143**, 4661–4667.

34 H. Tanaka, M. Ikenosako, Y. Kato, M. Fujiki, Y. Inoue and T. Mori, *Commun. Chem.*, 2018, **1**, 38.

35 X. Zhan, A. Facchetti, S. Barlow, T. J. Marks, M. A. Ratner, M. R. Wasielewski and S. R. Marder, *Adv. Mater.*, 2011, **23**, 268–284.

36 N. J. Schuster, R. H. Sánchez, D. Bukharina, N. A. Kotov, N. Berova, F. Ng, M. L. Steigerwald and C. Nuckolls, *J. Am. Chem. Soc.*, 2018, **140**, 6235–6239.

37 D. Aranda, N. J. Schuster, X. Xiao, F. J. Á. Ferrer, F. Santoro and C. Nuckolls, *J. Phys. Chem. C*, 2021, **125**, 2554–2564.

38 N. J. Schuster, L. A. Joyce, D. W. Paley, F. Ng, M. L. Steigerwald and C. Nuckolls, *J. Am. Chem. Soc.*, 2020, **142**, 7066–7074.

39 X. Xiao, S. K. Pedersen, D. Aranda, J. Yang, R. A. Wiscons, M. Pittelkow, M. L. Steigerwald, F. Santoro, N. J. Schuster and C. Nuckolls, *J. Am. Chem. Soc.*, 2020, **143**, 983–991.

40 B. Liu, M. Böckmann, W. Jiang, N. L. Doltsinis and Z. Wang, *J. Am. Chem. Soc.*, 2020, **142**, 7092–7099.

41 L. Zhang, I. Song, J. Ahn, M. Han, M. Linares, M. Surin, H.-J. Zhang, J. H. Oh and J. Lin, *Nat. Commun.*, 2021, **12**, 142.

42 W. Shi, F. Salerno, M. D. Ward, A. Santana-Bonilla, J. Wade, X. Hou, T. Liu, T. J. S. Dennis, A. J. Campbell, K. E. Jelfs and M. J. Fuchter, *Adv. Mater.*, 2021, **33**, 2004115.

43 G. Yu, J. Gao, J. C. Hummelen, F. Wudl and A. J. Heeger, *Science*, 1995, **270**, 1789–1791.

44 Y. Yang, R. C. Da Costa, D. M. Smilgies, A. J. Campbell and M. J. Fuchter, *Adv. Mater.*, 2013, **25**, 2624–2628.

45 L. Wan, J. Wade, X. Shi, S. Xu, M. J. Fuchter and A. J. Campbell, *ACS Appl. Mater. Interfaces*, 2020, **12**, 39471–39478.

46 J. Wade, J. N. Hilfiker, J. R. Brandt, L. Liirò-Peluso, L. Wan, X. Shi, F. Salerno, S. T. J. Ryan, S. Schöche, O. Arteaga, T. Jávorfi, G. Siligardi, C. Wang, D. B. Amabilino, P. H. Beton, A. J. Campbell and M. J. Fuchter, *Nat. Commun.*, 2020, **11**, 6137.

47 M. D. Ward, J. Wade, X. Shi, J. Nelson, A. J. Campbell and M. J. Fuchter, *Adv. Opt. Mater.*, 2021, 2101044.

48 L. Liu, Y. Yang, J. Zhang, W. Memon, Y. Zhang and Z. Wei, *Res. Square*, 2020, DOI: 10.21203/rs.3.rs-39893/v1.

49 M. Schulz, F. Balzer, D. Scheunemann, O. Arteaga, A. Lützen, S. C. J. Meskers and M. Schiek, *Adv. Funct. Mater.*, 2019, **29**, 1900684.

50 Z. Wang, M. Gao, X. Hao and W. Qin, *Appl. Phys. Lett.*, 2020, **116**, 053301.

51 N. Y. Kim, J. Kyhm, H. Han, S. J. Kim, J. Ahn, D. K. Hwang, H. W. Jang, B.-K. Ju and J. A. Lim, *Adv. Funct. Mater.*, 2019, **29**, 1808668.

52 X. Shang, I. Song, H. Ohtsu, Y. H. Lee, T. Zhao, T. Kojima, J. H. Jung, M. Kawano and J. H. Oh, *Adv. Mater.*, 2017, **29**, 1605828.

53 X. Shang, I. Song, J. H. Lee, W. Choi, J. Ahn, H. Ohtsu, J. C. Kim, J. Y. Koo, S. K. Kwak and J. H. Oh, *ACS Nano*, 2020, **14**, 14146–14156.

54 A. K. Jena, A. Kulkarni and T. Miyasaka, *Chem. Rev.*, 2019, **119**, 3036–3103.

55 J. Y. Kim, J.-W. Lee, H. S. Jung, H. Shin and N.-G. Park, *Chem. Rev.*, 2020, **120**, 7867–7918.

56 G. Long, R. Sabatini, M. I. Saidaminov, G. Lakhwani, A. Rasmita, X. Liu, E. H. Sargent and W. Gao, *Nat. Rev. Mater.*, 2020, **5**, 423–439.

57 J. Hao, H. Lu, L. Mao, X. Chen, M. C. Beard and J. L. Blackburn, *ACS Nano*, 2021, **15**, 7608–7617.

58 D. G. Billing and A. Lemmerer, *Acta Crystallogr.*, 2003, **E59**, m381–m383.

59 A. Ishii and T. Miyasaka, *Sci. Adv.*, 2020, **6**, eabd3274.

60 D. G. Billing and A. Lemmerer, *CrystEngComm*, 2006, **8**, 686–695.

61 J. Ahn, E. Lee, J. Tan, W. Yang, B. Kim and J. Moon, *Mater. Horiz.*, 2017, **4**, 851–856.

62 J. Ma, C. Fang, C. Chen, L. Jin, J. Wang, S. Wang, J. Tang and D. Li, *ACS Nano*, 2019, **13**, 3659–3665.

63 J. Wang, C. Fang, J. Ma, S. Wang, L. Jin, W. Li and D. Li, *ACS Nano*, 2019, **13**, 9473–9481.

64 J. Wang, H. Lu, X. Pan, J. Xu, H. Liu, X. Liu, D. R. Khanal, M. F. Toney, M. C. Beard and Z. V. Vardeny, *ACS Nano*, 2020, **15**, 588–595.

65 Y. Zhao, Y. Qiu, J. Feng, J. Zhao, G. Chen, H. Gao, Y. Zhao, L. Jiang and Y. Wu, *J. Am. Chem. Soc.*, 2021, **143**, 8437–8445.

66 D. Li, X. Liu, W. Wu, Y. Peng, S. Zhao, L. Li, M. Hong and J. Luo, *Angew. Chem., Int. Ed.*, 2021, **60**, 8415–8418.

67 L. Wang, Y. Xue, M. Cui, Y. Huang, H. Xu, C. Qin, J. Yang, H. Dai and M. Yuan, *Angew. Chem., Int. Ed.*, 2020, **59**, 6442–6450.

68 X. Zhang, X. Liu, L. Li, C. Ji, Y. Yao and J. Luo, *ACS Cent. Sci.*, 2021, **7**, 1261–1268.

69 D.-W. Zhang, M. Li and C.-F. Chen, *Chem. Soc. Rev.*, 2020, **49**, 1331–1343.

70 Y. Kitagawa, S. Wada, M. D. J. Islam, K. Saita, M. Gon, K. Fushimi, K. Tanaka, S. Maeda and Y. Hasegawa, *Commun. Chem.*, 2020, **3**, 119.

71 S.-H. Yang, R. Naaman, Y. Paltiel and S. S. P. Parkin, *Nat. Rev. Phys.*, 2021, **3**, 328–343.

72 P. Wang, I. Jeon, Z. Lin, M. D. Peeks, S. Savagatrup, S. E. Kooi, T. Van Voorhis and T. M. Swager, *J. Am. Chem. Soc.*, 2018, **140**, 6501–6508.

73 L. D. Barron, *Nat. Mater.*, 2008, **7**, 691–692.